Results in Engineering 31 (2026) 111258

Contents lists available at ScienceDirect

Results in Engineering

journal homepage: www.sciencedirect.com/journal/results-in-engineering

Research paper

Elaboration of 316L/Cu composite alloy using a hybrid PVD/SPS process

Yoann Pinot [a,*], Romaric Masset [a], Aurélien Besnard [b], Rémi Aubert [c], Guillaume Colas [c], Maria-Rosa Ardigo-Besnard [d], Florian Bussière [d]

[a] *Arts et Metiers Institute of Technology, LaBoMaP, 13 rue Porte de Paris, 71250 Cluny, France*
[b] *Université Marie et Louis Pasteur, SUPMICROTECH, CNRS, institut FEMTO-ST, F-25000 Besançon, France*
[c] *Université Marie et Louis Pasteur, CNRS, institut FEMTO-ST, F-25000 Besançon, France*
[d] *Université Bourgogne Europe, CNRS, Laboratoire Interdisciplinaire Carnot de Bourgogne ICB UMR 6303, F-21000 Dijon, France*

ARTICLE INFO

Keywords:
Hybrid PVD/SPS process
Powder metallurgy
Cu/316 L composite
Wear behavior
Physical vapor deposition (PVD)
Spark plasma sintering (SPS)

ABSTRACT

Powder metallurgy is an ideal field for developing advanced materials with complex geometries and compositions. While, iron-based alloys produced through Spark Plasma Sintering often exhibit residual porosity, adding small amounts of copper provides several benefits: it lowers the sintering temperature, eliminates pores due to its excellent wettability, reduces stress concentrations, and prevents microcracks formation. The localization of copper at the grain boundaries of steel powder particles enables the design of an alloy with a controlled microstructure, thus enhancing its mechanical performance as well as its resistance to corrosion and oxidation. The innovative hybrid approach presented in this work, combines Physical Vapor Deposition (PVD) and Spark Plasma Sintering (SPS) processes. In this study, the development of a 316 L alloy with copper-enriched powder particle boundaries is investigated. Surface functionalization of the powders is performed using an inhouse-designed PVD chamber with an original configuration. This synthesis method ensures more precise control over the amount and distribution of copper at the grain boundaries of the powder particles, making it easier to achieve a homogeneous material and enhanced optimization of its mechanical performance. The influence of the copper layer thickness on mechanical performance and on the microstructure after sintering is assessed using several characterization techniques. The bulk composite materials produced exhibit a network-type structure. Increasing the copper content beyond 0.52 wt.% leads to a rise in the elongation at break of the sintered samples. Although hardness tends to decrease slightly with copper addition, copper effectively reduces porosity except at very low concentrations.

1. Introduction

Powder metallurgy is an ideal field for the development of advanced materials with complex geometries and tailored compositions, capable of meeting the challenges and stringent requirements of the aerospace, automotive, and energy industries. The Spark Plasma Sintering (SPS) process is a shaping technology initially used for the high-temperature sintering of ceramics such as carbides, borides, silicides, and oxides [1–4]. It was later extended to metals and metallic alloys [5]. This process is also employed for joining ceramics or metals [6], fabricating composites [7], and producing thick coatings [8].

SPS enables the formation of fine-grained microstructures and high densification at lower temperatures and with much faster heating rates than conventional sintering techniques. Powder consolidation and densification result from the combined action of uniaxial pressure and pulsed electric current, which induce both plastic deformation and Joule heating. Electrical discharges generated at particle interfaces create a plasma that enhances thermal diffusion by removing adsorbed gases, impurities, and surface oxide layers [9]. Consequently, SPS allows the production of dense, high-performance materials in a single step, exhibiting excellent mechanical properties. The process is particularly well suited for producing materials with controlled microstructures, such as duplex alloys [10] or metal-matrix composites [11], which combine the advantages of different material families while offering great flexibility in microstructural control. This capability is especially valuable for systems where a secondary metallic phase is introduced, such as 316 L steel composites incorporating copper. For 316 L steel-matrix composites with a copper binder, the addition of Cu can

---

* Corresponding author.

E-mail addresses: yoann.pinot@ensam.eu (Y. Pinot), romaric.masset@ensam.eu (R. Masset), aurelien.besnard@femto-st.fr (A. Besnard), remi.aubert@femto-st.fr (R. Aubert), guillaume.colas@femto-st.fr (G. Colas), maria-rosa.ardigo-besnard@ube.fr (M.-R. Ardigo-Besnard), florian.bussiere@ube.fr (F. Bussière).

https://doi.org/10.1016/j.rineng.2026.111258
Received 4 March 2026; Received in revised form 15 May 2026; Accepted 26 May 2026
Available online 27 May 2026
2590-1230/© 2026 The Author(s). Published by Elsevier B.V. This is an open access article under the CC BY license (http://creativecommons.org/licenses/by/4.0/).

enhance mechanical properties [12] (ductility, wear resistance), physical properties [13] (electrical and thermal conductivity), corrosion resistance [14], and may even impart antibacterial effects [15]. Moreover, copper offers several advantages during sintering: it lowers the sintering temperature, eliminates pores thanks to its excellent wettability, reduces stress concentrations, and prevents microcrack formation [16].

Several approaches can be used to produce Cu/316 L composite materials via powder metallurgy: additive manufacturing [13,17], infiltration of liquid copper into a compacted steel preform [18], or sintering of mixed steel and copper powders [16]. However, these methods face limitations, particularly in controlling the copper content at low concentrations, and they require a phase change (Cu melting) to ensure proper densification. Liquid copper infiltration often leads to heterogeneous distribution due to variations in residual porosity [18], while sintering powder mixtures may result in heterogeneous microstructures with copper islands or clusters [16].

This work introduces an innovative hybrid approach combining physical vapor deposition (PVD) on powder with spark plasma sintering (SPS) to produce bulk materials with controlled microstructures. This method enables precise control of the amount and distribution of copper at powder interfaces, with or without melting, thereby promoting improved homogeneity and optimized performance. Plasma-based technologies can indeed be used to functionalize granular materials at the nano- or microscale [10,19]. In this study, we focus on a well-established 316L/Cu model system from the literature to evaluate the feasibility of producing materials with controlled microstructures, such as metal matrix composites (MMCs), ceramic matrix composites (CMCs), and ceramic materials with a metallic blinder (CERMETs), using this hybrid process. The influence of the copper coating thickness on the powder—both before and after sintering—on the microstructure and mechanical properties of the 316L/Cu composite is investigated. Thereby, micrometer-sized 316 L austenitic stainless-steel powder (250–300 μm in diameter) was coated with copper by sputter deposition and subsequently sintered. Surface functionalization of the powders is performed using a custom-designed PVD chamber prototype developed in-house. The mechanical performance and microstructure of the consolidated material were evaluated as a function of the deposited copper film thickness (ranging from around 100 to 1000 nm), which can be associated with an equivalent copper content in the final material. The microstructure and phase identification of the coated powder and the sintered samples were studied using scanning electron microscopy (SEM), energy dispersive X-ray spectroscopy (EDS), and X-ray diffraction (XRD). The mechanical behavior of the sintered samples was characterized through tensile testing, hardness measurements and wear tests.

2. Materials and method

2.1. Magnetron sputtering

The austenitic stainless steel AISI 316 L powder supplied by Aubert & Duval (France) was produced by gas atomization. Its nominal chemical composition provided is as follows: 0.015 wt.% C – 17.7 wt.% Cr – 1.88 wt.% Mn – 11.9 wt.% Ni – 2.44 wt.% Mo – 0.83 wt.% Si – 0.0117 wt.% O – balance Fe. The particle size was selected by sieving and ranges from 250 to 300 μm. Each processed powder batch corresponds to a mass of 30 g.

The copper coating on the 316 L powder particles was synthesized by DC magnetron sputtering using a circular copper target (diameter 50.8 mm, thickness 6 mm, purity 99.99 %). The magnetron system is positioned at the top of the chamber so that the atomic flux emitted from the target is vertical, moving from top to bottom.

A blade wheel serves as a container to hold and agitate the powder, ensuring complete and homogeneous coverage of each individual particle during deposition. Its rotation axis is inclined at 60° relative to the normal of the target surface (Fig. 1), which facilitates mixing while keeping the powder inside the wheel by gravity. The wheel has a diameter of 110 mm, a depth of 45 mm, and an opening area of 3.85 × 10^{-3} m^2. The rotation speed is set to 30 rpm. Before deposition, the chamber was pumped down to a residual pressure of 3 × 10^{-6} mbar. The working pressure was then set to 5.6 × 10^{-3} mbar by introducing argon at a flow rate of 5 sccm. The discharge current was set to 100 mA with the target voltage was held at −400 V.

2.2. Spark plasma sintering

Sintering was carried out using an SPS HPD 10 device (FCT Systeme GmbH). A cylindrical graphite die (inner diameter: 30 mm, outer diameter: 90 mm, height: 50 mm, Fig. 2.a) was filled with approximately 30 g of 316 L stainless steel powder to obtain, after sintering, a solid disk 30 mm in diameter and 6 mm in height. The powder was not precompacted. The sintering cycle consisted of an initial dwell at 1000 °C for 5 min to sinter the powder without inducing copper melting (Tm = 1085 °C), followed by a second dwell at 1050 °C for 10 min to promote consolidation and reduce porosity. The entire process was carried out under vacuum (~10^{-2} mbar) with a uniaxial pressure of 70 MPa (Fig. 2.b). The average punch displacement was 4.2 mm. The heating and cooling rates were 50 °C/min and >100 °C/min, respectively.

2.3. Sample preparation and characterization

After sintering, the samples were cut using a Buehler Isomet 4000 precision saw, mounted in resin, and polished with SiC abrasive papers up to 1200 grit, followed by polishing with diamond suspensions from 9 to 1 μm using a Buehler Beta polisher equipped with a Vector head. Porosity was measured on transverse sections using multiple optical microscopy images (Olympus BX51M), complemented by image processing (binarization) with ImageJ®.

Both the powders and the sintered bulk materials were analyzed using a JEOL JSM-7610F field-emission scanning electron microscope (SEM), coupled with an EDS detector (X-Max, Oxford Instruments) for elemental analysis at 20 keV. Coating thicknesses were determined by secondary-electron SEM imaging on powders previously embedded in epoxy resin and polished to obtain cross-sectional views. Approximately ten measurements were performed per powder batch. Phase identification was carried out by X-ray diffraction (XRD) in Bragg-Brentano θ–2θ configuration using a Bruker D8-25A Advance diffractometer with Cu Kα radiation (λ = 1.54056 Å).

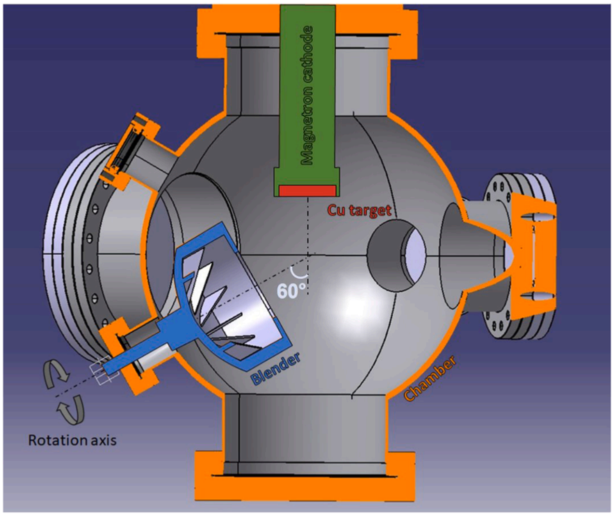

Fig. 1. Transverse schematic view of the PVD deposition chamber with the magnetron cathode and the mixing wheel.

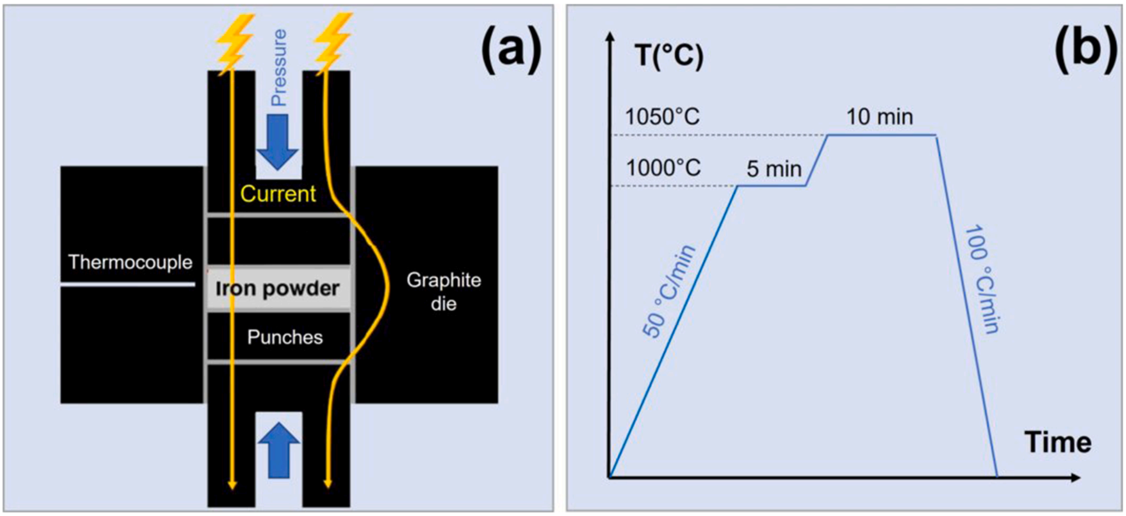

Fig. 2. (a) Transverse illustration of the SPS setup; (b) Graphical representation of the thermal profile experienced by the powder during the sintering process.

Vickers microhardness measurements were performed on transverse sections using a Vickers indenter and a 1 kgf load with a Wilson Tukon 1102/1202 hardness tester. Tensile tests were conducted using a Lloyd Instruments LR 30k machine equipped with an optical extensometer. Tests were performed at room temperature with a crosshead speed of 1 mm/min. The tensile specimens, machined from the sintered disk, has a dog-bone-shaped geometry, closely matching the specifications of NF EN ISO 6892 or ASTM E8. The specimens had a total length of 25 mm with a thickness of 5 mm, a gauge length of 10 mm, and a gauge section of 15 mm² (5 mm × 3 mm). Fracture surfaces were examined by SEM.

Wear resistance and friction behavior were evaluated using a reciprocating linear tribometer (R-Tec MFT 5000). A 6-mm-diameter WC/Co ball was used in pure sliding, under dry conditions, against samples polished to 1 μm diamond paste. Temperature and humidity were maintained at 20–22 °C and 55–65 % RH, respectively. The test was performed under a normal load of 4 N (corresponding to a maximal Hertz contact pressure of 1 GPa) for 1200 cycles (2400 passes), over a 4 mm stroke at a sliding speed of 3 mm/s. Data were recorded at 1000 Hz. Wear tracks and debris were characterized by SEM-EDS at 5 kV. The depth of the wear tracks was measured using an optical profilometer (Wyko NT 1100, Bruker).

3. Results and discussion

3.1. Characterization of the Cu-coated powder

The evolution of the coating thickness on the powder particles as a function of deposition time follows a linear trend (Fig. 3.a), which is commonly observed for films produced by PVD processes. The standard deviations increase with coating thickness, corresponding to a measurement uncertainty that remains roughly constant, between 10 and 20 % of the average thickness.

The deposition rate is 16.3 nm/h, corresponding to the slope of the fitted line. This rate is approximately 19 times lower than that measured for deposition on a static flat substrate (310 nm/h). Under fixed deposition conditions (working pressure, target-substrate distance, target current), the deposition rate depends on the rotation speed, the amount of powder, and the geometry of the particles (size, shape, distribution). These parameters influence the total surface area to be coated, the degree of particle overlap, and the average exposure time of the powder to the incident flux.

The strong reduction in deposition rate between powder and flat substrate is mainly explained by the large total surface area of the powder.

The particle volume is calculated at $V = 1.089 \times 10^{-11}$ m^3 using Eq. (1) based on an average powder diameter of $d = 275 \times 10^{-6}$ m. To

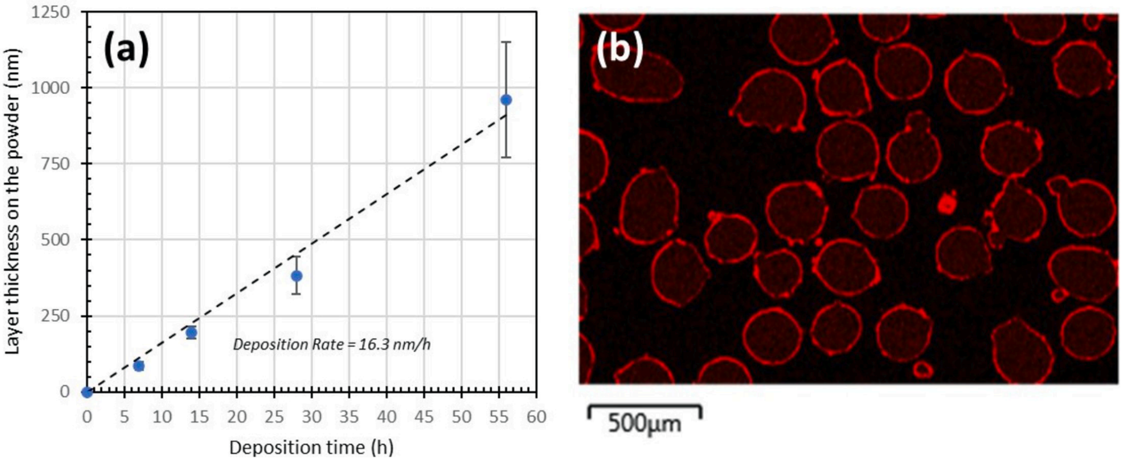

Fig. 3. (a) Graphical representation of the coating thickness evolution as a function of deposition time on the powder; (b) EDS mapping of copper in a transverse cross-section of a 316 L powder particle coated with a Cu layer after 56 h of deposition.

simplify the analytical treatment and ensure the applicability of Eq. (1), the particles are assumed to be perfectly spherical.

$$V = \frac{\pi}{6} d^3 \tag{1}$$

The number of powder particles is estimated from the total powder mass ($m = 30 \times 10^{-3}$ kg), the particle volume V, and the density of 316 L stainless steel ($\rho_{316L} = 7980$ kg/m^3), leading to $n = 345{,}240$ using Eq. (2).

$$n = \frac{m}{V.\rho_{316L}} \tag{2}$$

The total surface area of the powder is then estimated by multiplying the number of particles by the surface area of a spherical particle, yielding $s = 0.082$ m^2 (Eq. (3)).

$$s = n.\pi d^2 \tag{3}$$

The atomic incident flux passing through the opening area of the rotating wheel is derived from the deposition rate measured on a flat substrate (DR = 310 nm/h) and the opening area of the rotating wheel ($A = 3.85 \times 10^{-3}$ m^2). The flux is estimated as $f = 6.1 \times 10^{19}$ atoms/h using Eq. (4), by converting the deposited volume into an atomic flux assuming an approximate atomic volume based on the copper atomic diameter ($d_{Cu} = 270$ pm).

$$f = \frac{DR.A}{d_{Cu}.d_{Cu}^2} \tag{4}$$

The number of copper atoms required to form a monolayer on the powder ($c = 1.12 \times 10^{18}$ atoms) is determined from the total surface area s, assuming a simplified atomic packing (Eq. (5)).

$$c = \frac{s}{d_{Cu}^2} \tag{5}$$

Assuming that all incident atoms uniformly cover the powder surface over time, the effective deposition rate on the powder is estimated by relating the incoming atomic flux to the number of atoms required to form a monolayer. This yields a calculated deposition rate of approximately 15 nm/h (Eq. (6)). This represents an ideal lower-bound estimation, as shadowing effects and particle rearrangement are not considered.

$$DR_{calculated} = \frac{f.d_{Cu}}{c} \tag{6}$$

This value is very close to the experimentally measured rate (Fig. 3.a), highlighting the major influence of the powder's specific surface area on the deposition rate. All coated powder batches exhibit a uniform coating thickness and homogeneous coverage across all particles, as illustrated by the EDS mapping in Fig. 3.b for a powder treated for 56 h. Local EDS analyses performed at 5 kV on the surface of the uncoated powder show an oxygen content of 1.8 wt.% ± 1.2 in the steel. In contrast, the coated powder exhibits a slightly higher oxygen content of 2.1 wt.% ± 0.3, along with a copper content of 97.4 wt.% ± 0.5**.** At this accelerating voltage, the interaction volume probes mainly the copper layer, indicating that the Cu coating contains only a low level of oxygen contamination compared with the raw powder.

The morphology of the raw 316 L powder is predominantly spherical, with satellites attached to the surface and exhibiting diameters ranging from 10 to 100 µm (Figure 4.a). The transverse cross-section (Figure 4.d) shows an interface (resin/316 L) without coating or thick oxide layer. Figure 4.b shows the presence of a dendritic structure. The morphology and microstructure of the powder are therefore directly related to the atomization process used for its production. High-magnification observation reveals a relatively smooth surface with the presence of micro-droplets (Fig. 4.c). SEM images of the 316 L powder coated with copper after 28 h of deposition show an overall homogeneous coverage, although local delamination occurs in highly stressed areas due to the presence of satellites (Fig. 4.f). At low magnification (*e.g.*, × 100), it is not possible to visually distinguish the coated powder (Fig. 4.e) from the uncoated one (Fig. 4.a). The transverse cross-section (Figure 4.h) indicates a coating thickness on the order of several hundred nanometers, typically exhibiting a columnar microstructure [10]. Fig. 4.g shows the surface of the copper film in top view at high magnification (× 60 000), where nodules with diameters of approximately 10–20 µm can be observed.

3.2. *Microstructural evolution after sintering*

Fig. 5.a shows the evolution of the bulk composition after sintering as a function of the deposition time on the powder particles. The red curve corresponds to the theoretical calculation, while the blue curve is derived from the experimental EDS data. The theoretical values are calculated using Eq. (7) with the masses of copper (m_{Cu}) and steel (m_{316L}). The masses of copper and steel are determined respectively using $\rho_{Cu} = 8960$ kg/m^3; $\rho_{316L} = 7980$ kg/m^3; particle diameter $d = 275 \times 10^{-6}$ m; film thickness $e = 163 \times 10^{-10} \cdot t$ m, where the deposition time t is expressed in hours.

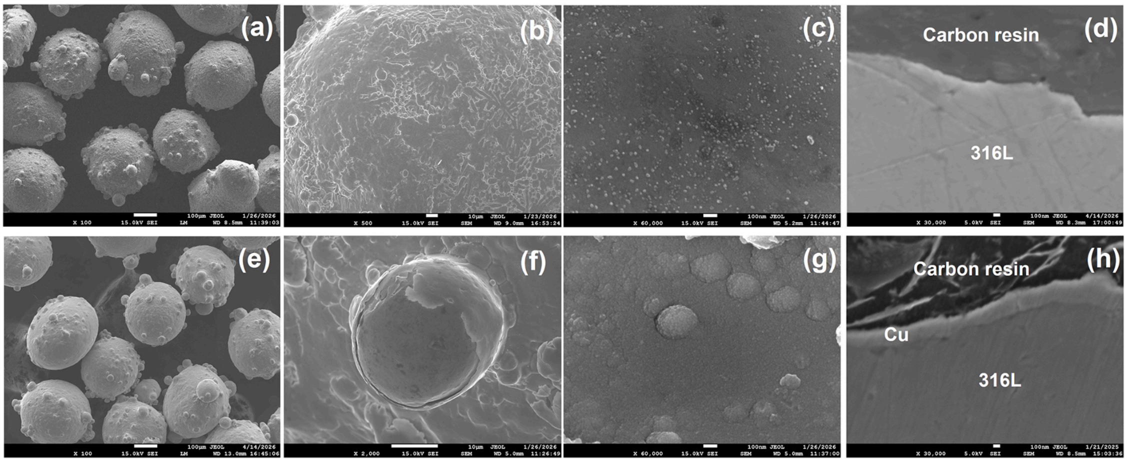

Fig. 4. SEM images of the 316 L powder top view at magnifications of × 100, × 500, and × 60,000 for (a), (b) and (c), respectively. SEM images of the 316 L powder coated with a Cu layer after 28 h of deposition top view at magnifications of × 100, × 500, and × 60,000 for (e), (f), and (g), respectively. Transverse cross-section at × 30,000 for the 316 L powder and the 316 L powder coated with a Cu layer: (d) and (h), respectively.

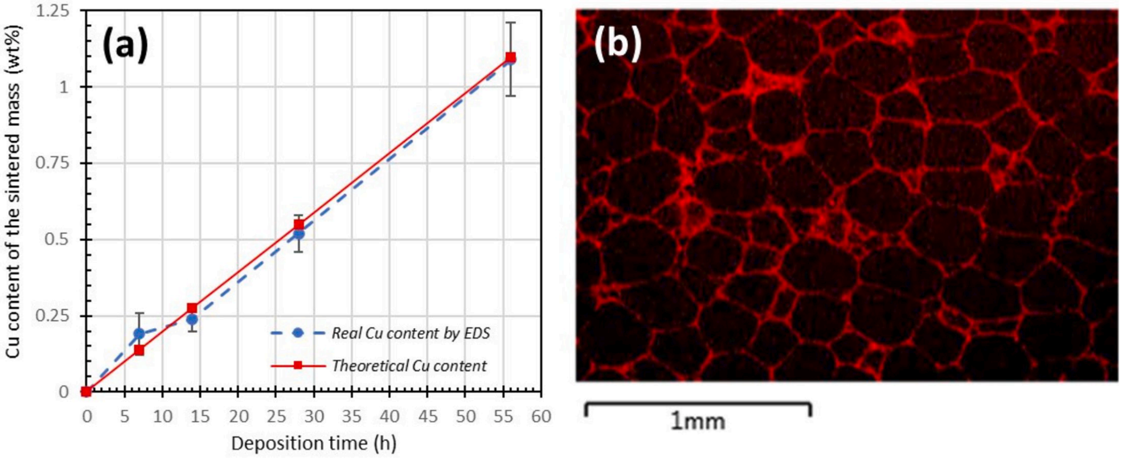

Fig. 5. (a) Graphical representation of the evolution of the copper content in the bulk material after sintering as a function of the deposition time applied to the powder prior to sintering; (b) EDS mapping of copper in a transverse cross-section of a sintered bulk sample produced from 316 L powder coated for 56 h.

$$wt.\%_{Cu} = \left(\frac{m_{Cu}}{m_{Cu}+m_{316L}}\right).100 = \left(\frac{\frac{\pi}{6}\left[(d+2e)^3-d^3\right].\rho_{Cu}}{\frac{\pi}{6}\left[(d+2e)^3-d^3\right].\rho_{Cu}+\frac{\pi}{6}d^3.\rho_{316L}}\right).100 \qquad (7)$$

The EDS analyses are consistent with the theoretical values calculated from the deposition rate. The bulk composition as a function of deposition time on the powder follows a linear trend. All batches of coated and sintered powders exhibit a composite alloy microstructure consisting of steel cells bordered by Cu-rich regions, as shown by the copper EDS mapping for the powder coated for 56 h and subsequently sintered (Fig. 5.b). The size of these cells is close to the initial diameter of the powder particles, i.e., 250–300 µm.

The rapid sintering at lower temperatures compared to conventional sintering processes allows the SPS technique to limit copper diffusion into the steel, thereby preserving the original powder particle boundaries. This effect is further enhanced by the immiscibility of copper with most of the alloying elements present in steel. However, the interfacial structure remains complex. A sub-cellular network, approximately ten micrometers in size, can be observed propagating into the steel powder from the powder particle boundaries (Fig. 6). The presence of this subnetwork may be attributed to the dendritic structure of the atomized powder. Copper would then preferentially diffuse along the interdendritic regions, which are enriched in alloying elements exhibiting strong affinity with copper, such as nickel. This implies the Cu diffusion occurs very fast, before the dendritic structure vanishes under the heating effect. Bright spots can be seen on the EDS map, indicating areas with a very high copper content. These features may correspond to remnants of the original copper layer.

Fig. 7 shows the EDS mapping in a transverse cross-section of the sintered bulk material produced from powder coated for 56 h. The EDS maps in the powder particle boundary regions reveal the presence of oxide inclusions enriched in Si and Mn, which may correspond to silica or a mixed oxide. XRD analysis did not allow these inclusions to be identified due to their very small size and low concentration in the material. The presence of such oxide inclusions is common in stainless steels [20]. It is also observed that Fe, Cr, and Mo remain localized within the steel matrix. This is consistent with the fact that copper is immiscible, or only weakly miscible with these elements, whereas nickel mixes readily with copper. The oxygen content in the bulk material remains similar regardless of copper concentration (between 0.6 and 0.8 wt.%), indicating that the coating process does not introduce significant oxygen contamination, in agreement with local EDS analyses on the surface of the coated powder.

Table 1 presents the compositional analyses performed in the copper-poor regions, corresponding to the steel powder, and in the copper-rich powder particle boundary regions. The composition measured in the powder is consistent with that of a 316 L austenitic stainless steel [21, 22]. In the copper-rich powder particle boundary regions, a decrease in

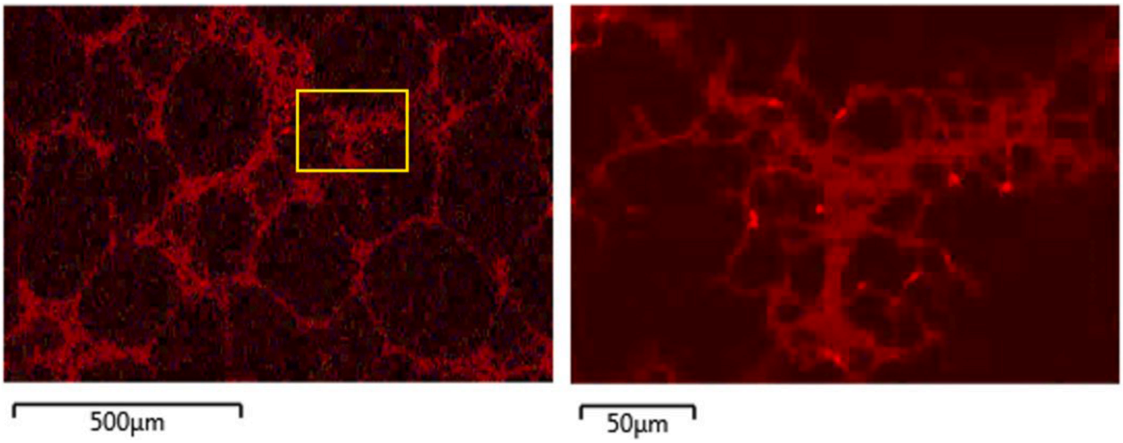

Fig. 6. EDS maps of copper in a transverse cross-section of a sintered bulk sample produced from powder coated for 28 h; magnification of the yellow-highlighted region.

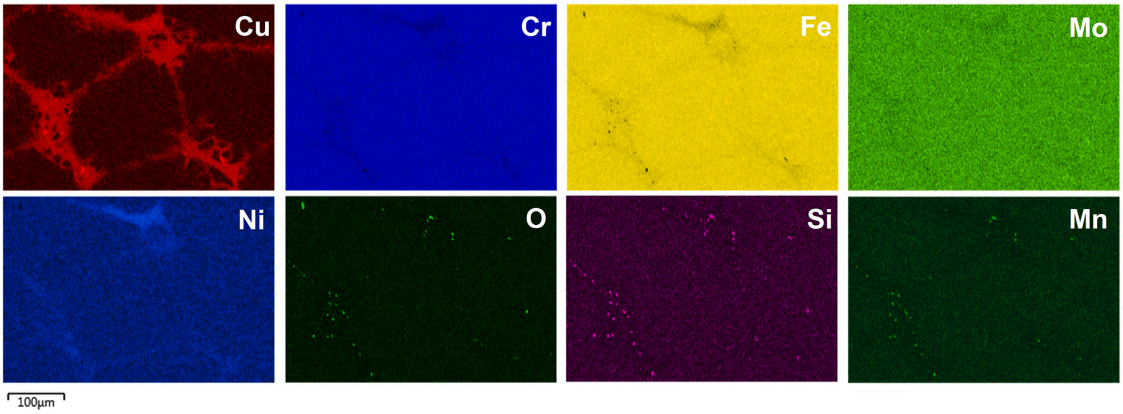

Fig. 7. Transverse EDS maps of the different elements present in a sintered bulk material produced from powder coated with copper for 56 h.

Table 1
Mass fractions of the elements present in the powder particle boundaries (copper-rich region) and inside the powder particle (copper-poor region) of a sintered bulk material produced from 316 L powder coated with copper for 28 h.

Wt.%	Fe	Ni	Cr	Cu	Mo	Mn	Si	O
Cu-rich area	51.0 ± 0.9	22.2 ± 0.9	14.1 ± 0.5	8.4 ± 1.0	1.7 ± 0.2	1.7 ± 0.5	0.6 ± 0.0	0.4 ± 0.0
Cu-poor area	63.4 ± 0.9	14.0 ± 0.3	17.9 ± 0.3	0.0 ± 0.0	2.3 ± 0.5	1.2 ± 0.2	0.8 ± 0.1	0.4 ± 0.0

Fe, Cr, Mo, and Si is observed, in agreement with the observations in Fig. 7. Conversely, the Ni, Cu, and Mn contents increase. The compositional difference between the copper-rich and copper-poor regions allows an estimation of the powder particle boundary composition after sintering. The normalized composition is 50.3 wt.% Ni, 46.4 wt.% Cu, and 3.3 wt.% Mn.

The crystallographic analyses (Fig. 8.a) were performed on three samples: uncoated 316 L powder, 316 L powder coated with copper for 56 h, and a bulk material sintered with Cu-coated powder. The phases were indexed using the ICDD reference cards from the EVA database: austenite (00-033-0397, stainless steel, fcc, 3.59866 Å), ferrite (00-054-0331, stainless steel, bcc, 2.87050 Å), and copper (04-009-2090, fcc, 3.60350 Å).

All diffractograms show the presence of a face-centered cubic austenitic phase, with no detectable texture, similar to a typical powder diffraction pattern. The (111), (200), and (220) peaks appear at 2θ = 43.54°, 50.68°, and 74.53°, respectively. A splitting of the sharp and intense peaks is observed, corresponding to the $K\alpha_2$ component of the X-ray source.

The average lattice parameter is $a_c = 3.593$ Å. The average crystallite size (L) was calculated using the Scherrer Eq. (8), where λ is the X-ray wavelength, β the full width at half maximum of the diffraction peak, and θ the diffraction angle. β and θ are expressed in radians.

$$L = \frac{0.9\lambda}{\beta\cos\theta} \tag{8}$$

The average crystallite size was calculated for the (111) domains, corresponding to the most intense diffraction peak. The coherence lengths obtained are L_{111} = 460 Å, 468 Å, and 456 Å for the 316 L powder, the Cu-coated 316 L powder, and the sintered sample, respectively. This indicates that the crystallite size changes very little during

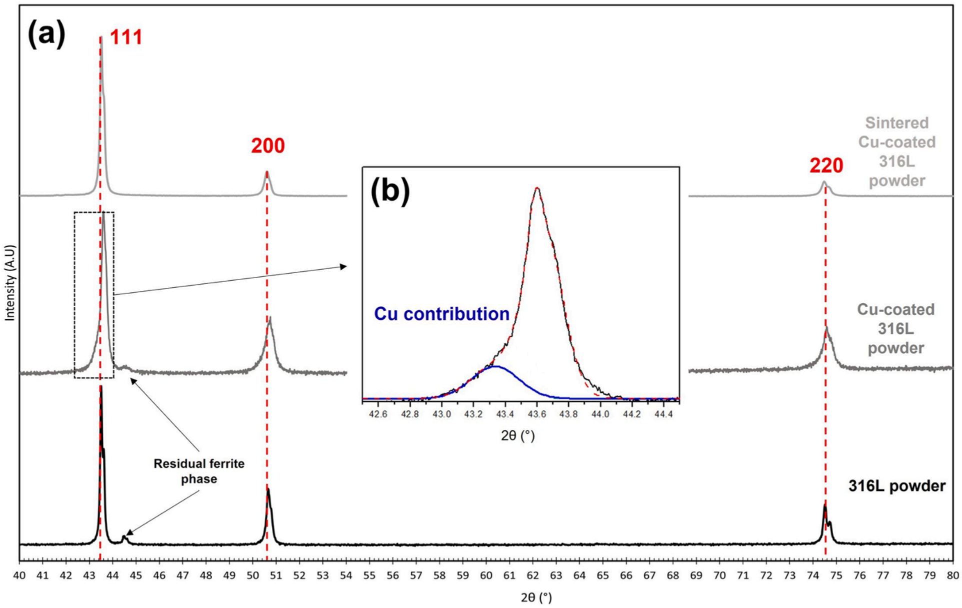

Fig. 8. X-ray diffractograms of the as-received 316 L powder, the 316 L powder coated with copper for 56 h, and the sintered bulk material produced from 316 L powder coated with copper for 56 h.

sintering.

Fig. 8.b shows a magnified view of the (111) peak of the Cu-coated 316 L powder. A shoulder is observed at 2θ = 43.33°, associated to the copper peak, demonstrating that the deposited layer is crystallized. The calculated lattice parameter is 3.614 Å, a value higher than that of the austenitic phase but consistent with the ICDD reference data. The associated coherence length is L_{111} = 183 Å. This relatively small value, typical of thin films, is attributed to the thinness of the coating (approximately 1 μm), which limits the crystallite domain size.

Both the 316 L powder and the Cu-coated 316 L powder exhibit a residual ferrite phase at 2θ = 44.70°, corresponding to the (110) family of planes. This residual ferrite disappears after the sintering process.

3.3. Mechanical performance of the sintered parts

Fig. 9.a shows the evolution of Vickers hardness as a function of copper content. A slight decrease in steel hardness is observed as the Cu content increases. The hardness of the copper-free steel is 175 HV, which is consistent with the literature. Kurgan *et al.*, [22] report hardness values between 110 and 200 HV depending on porosity levels in conventionally sintered 316 L, while Marnier *et al.*, [23] report values between 209 and 237 HV for flash-sintered 316 L.

A minimum hardness of 153 HV is reached at 0.52 wt.% Cu. Beyond this concentration, the hardness stabilizes, forming a plateau. Conventionally sintered copper–zinc alloys also exhibit relatively low hardness values, around 100 HV [24], which supports the trend observed here. However, the overall variation remains small (about 20 HV), due to the low copper contents studied (< 1.09 wt.% Cu). Fig. 9.b shows the evolution of porosity as a function of copper content. The measured values remain low compared with those typically observed in conventional sintering (5–20 % [16,25]) and are consistent with flash-sintering results (0.5–2.5 % [22,26]). At low Cu contents, porosity slightly increases from 0.75 % (Cu-free steel) to 1 % at 0.19 wt.% Cu. It then gradually decreases to 0.43 % at 1.09 wt.% Cu. The initial increase in porosity may be related to changes in the electrical behavior of the powder during sintering, leading to local heterogeneities at the powder particle interfaces. However, this trend reverses as the Cu content increases: at 1.09 wt.% Cu, porosity is low, indicating improved consolidation. A higher copper content enhances electrical contact at powder particle boundaries and acts as a binder due to its low plastic deformation resistance and low melting temperature. These results indicate that a minimum copper content — or at least a minimum coating thickness — is required to fully benefit from copper addition.

The stress–strain curves obtained from the tensile tests are shown in Fig. 10.a. These curves illustrate the evolution of stress as a function of specimen elongation. Fig. 10.b displays the variation of Re and Rm with

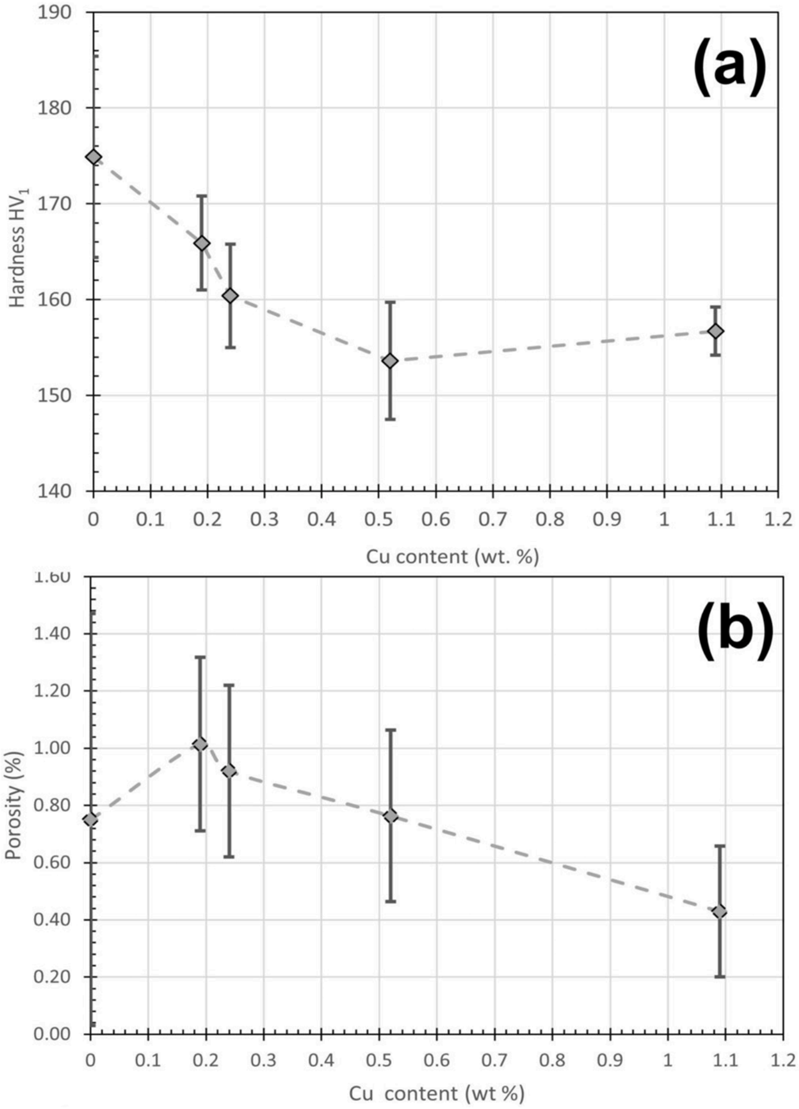

Fig. 9. Graphical representation of the evolution of (a) hardness and (b) porosity percentage as a function of Cu content in the sintered bulk material.

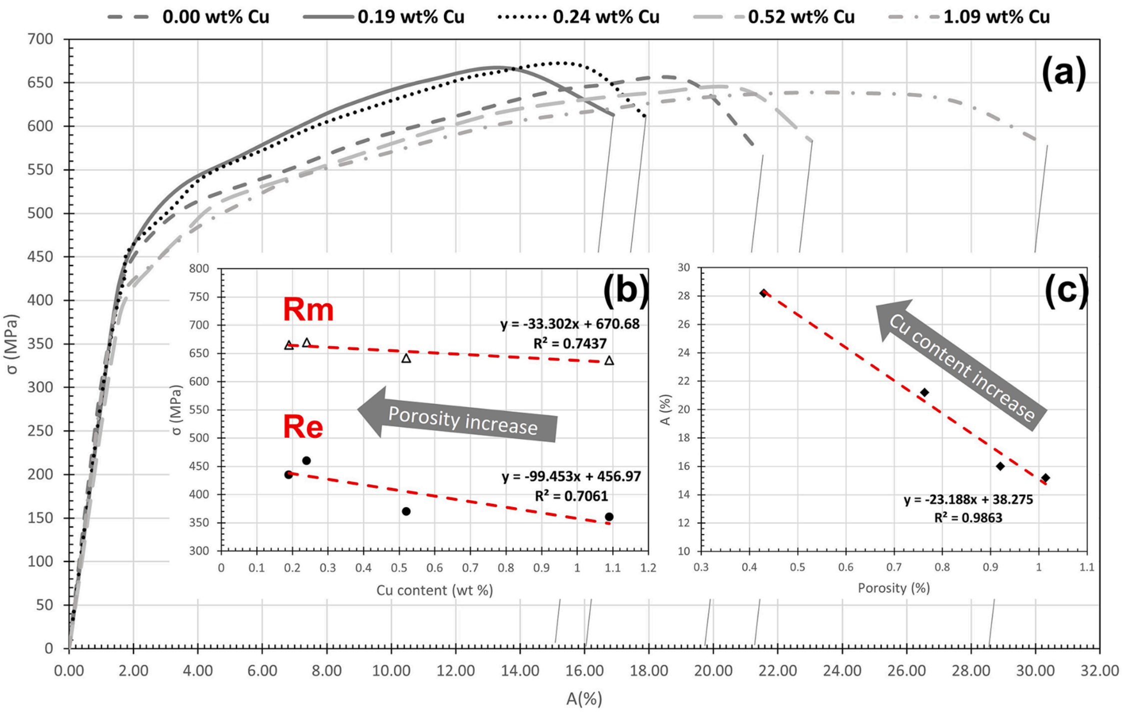

Fig. 10. (a) Tensile test curves showing the evolution of stress as a function of elongation percentage for sintered specimens with different copper contents; (b) Re and Rm as a function of the Cu content; (c) A% as a function of the porosity.

copper content, while Fig. 10.c shows the evolution of elongation at break as a function of porosity percentage. The mechanical properties (Re, Rm, and A%) of the specimens appear to follow a linear trend with respect to copper content or porosity level. The reference 316 L sample exhibits a yield strength of Re = 450 MPa, an ultimate tensile strength of Rm = 650 MPa, and an elongation at fracture of 19.6 %. These values are consistent with the literature [21,26,27]. Kale *et al.*, [21] reported a yield strength close to 400 MPa and ultimate strengths between 609 and 681 MPa for 316 L produced by flash sintering. Lokeshraj *et al.*, [26] studied the mechanical behavior of 316 L processed by SPS and SLM: additive manufacturing yielded Re = 505 MPa, Rm = 686 MPa, and A = 28 %, whereas SPS produced a more ductile material with Re = 303 MPa, Rm = 537 MPa, and A = 39 %.

Our results are consistent with those of the literature mentioned above, but fall on the lower end of the reported elongation values. This may be due to non-optimal sintering conditions, such as insufficient temperature or time, leading to partial neck formation between powder particles and promoting porosity. Kurgan *et al.*, [22] observed similar fracture morphologies, where the initial powder geometry remains visible after conventional sintering at 1200 °C and 800 MPa. In our case, the powder grain morphology is clearly visible in the fracture surface (Fig. 11), confirming partial sintering. Indeed, typical sintering temperatures for 316 L exceed 1100 °C, which was not the case in the present study. The lower temperature (1050 °C) was chosen to avoid copper melting during sintering (Tm = 1085 °C).

For low copper contents (0.19 and 0.24 wt.% Cu), a reduction in elongation at fracture is observed (15.2 % and 16 %, respectively) compared with uncoated 316 L (Fig. 10.a). This decrease is accompanied by a slight increase in Re ≈ 470 MPa and Rm ≈ 670 MPa, although the effect remains limited (Fig. 10.a). The higher porosity observed at these Cu contents (Fig. 9.b) likely contributes to the reduced sample elongation (Fig. 10.c). The slight increase in *Re* and Rm may be attributed to inclusions at powder particle boundaries or surface oxides, which can increase local stress fields through pinning effects [21], thereby reducing ductility.

The fracture surfaces of the three samples (316 L, 0.19 and 0.24 wt.% Cu) show circular regions composed of small dimples corresponding to necks formed between powder particles, indicative of ductile behavior (Fig. 11). These areas are bordered by smooth, angular regions associated with brittle zones rich in micro-voids, which promote crack

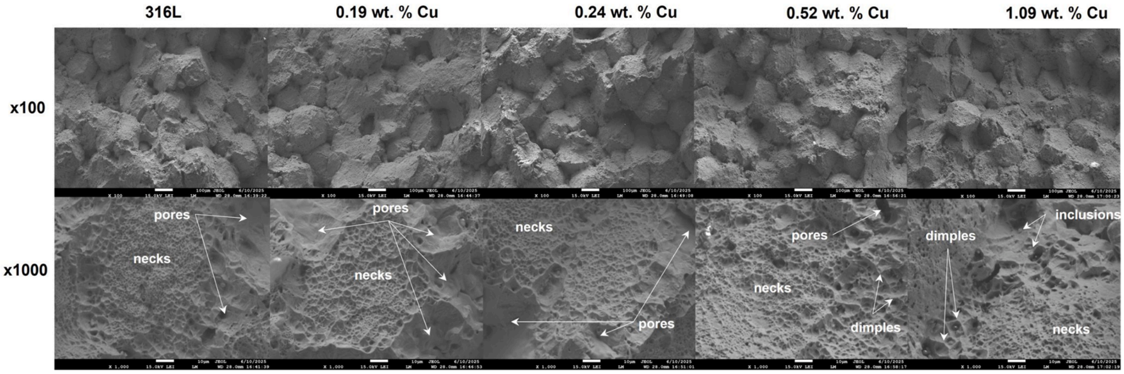

Fig. 11. Secondary-electron SEM images at × 100 and × 1000 of the fracture surfaces of tensile specimens from sintered samples with different copper contents.

initiation. The amount, size, shape, and distribution of porosity in the sintered bulk are key factors influencing the mechanical behavior of powder metallurgy materials [28]. It is established that increasing the sintering temperature generally reduces porosity and tends to make pores more spherical. However, in SPS, the presence of a liquid phase must be avoided to maintain good control of the process cycle. In the present study, the copper melting point was the main factor limiting the increase of the temperature.

For higher copper contents (0.52 and 1.09 wt.% Cu), an increase in elongation at fracture is observed compared with 316 L, reaching 21.2 % and 28.2 %, respectively. This increase in ductility is accompanied by a slight decrease in yield strength (Re ≈ 410 MPa) and ultimate tensile strength (Rm ≈ 640 MPa), which is consistent with the reduction in porosity (Fig. 9.b). Since copper is much more ductile than 316 L (Re = 110 MPa; Rm = 250 MPa; A = 48 % [29]), the increase in elongation (Fig. 10.c), results directly from the higher Cu content. Fig. 11 also shows circular regions composed of small dimples surrounded by larger ones, corresponding to copper-rich powder particle boundaries, illustrating a ductile fracture mode. The presence of larger dimples in these areas may be attributed to the presence of sizeable inclusions.

These results demonstrate that even low Cu contents can influence the mechanical behavior of sintered samples—particularly elongation at fracture—due to the homogeneous distribution of copper at powder particle boundaries. However, a minimum amount of copper, and therefore a minimum coating thickness, is required to produce this effect. The Cu content necessary to enhance the elongation at break of the 316 L tensile specimens is 0.52 wt.%, which corresponds to a coating thickness of approximately 450 nm for a particle diameter of 275 µm, as shown in Figs. 3, 4 and 10.

The tribological tests show a similar evolution for all samples (Fig. 12). The friction coefficient reaches a steady-state value of about 0.5 after a running-in period of approximately 100 cycles (Fig. 12). This average friction coefficient is consistent with previous studies [30]. The copper contents in the samples do not appear to affect the friction coefficient, likely because they are too low to significantly influence the tribological behavior.

The presence of copper does not appear to alter the wear behavior, which mainly occurs through the formation of powder and debris (Fig. 13.a.c). The wear surfaces are comparable across all samples, showing oxidized areas in the form of flakes and particles along the wear track (Fig. 13.b.d). Only the samples with the extreme composition, *i.e.*, 316 L and the 316 L with 1.09 wt.% Cu, are shown in Fig. 13 to clarify the analyses.

EDS analyses performed on the wear track of the 316 L and 316 L containing 1.09 wt.% Cu steel indicates a stoichiometry that could suggest the formation of hematite $(Fe,Cr)_2O_3$ in zone 1 (Table 2), corresponding to the plate-like features at the bottom of the track [30]. The debris is pushed toward the edges and within the wear track. The wear-track profiles exhibit parabolic shapes with visible grooves formed as a consequence of abrasive oxide particles (Fig. 13.a.c). Zones 2 shows oxygen contents to 12.5 wt.% (1.09 wt.% Cu) and 24.5 wt.% (316 L), suggesting partial oxidation of the debris, compared to zones 1. EDS analyses of the grooves within the wear track show a low oxygen content (Table 2, zones 3), regardless of the sample. This indicates that the material is exposed, with no oxide surface layer present. For 316 L, Zone 4 located outside the wear track, displays a composition similar to that of 316 L (Table 1). For the copper-doped 316 L steel, the copper contents measured in the debris are consistent with the overall Cu content initially measured in the sample (Table 1) and with those found in the weakly oxidized areas (1.09 wt.% Cu – zone 3) or in the ones without oxidation (1.09 wt.% Cu – zone 4).

The wear track depths of the doped (track depth: 9.2 µm and track width: 460 µm) and undoped (track depth: 10 µm and track width: 490 µm) steels show no significant difference, indicating an equivalent wear volume. The wear rate K_V is calculated with the following formula (9), where it is assumed that the volume loss V is proportional to the normal load ($F_N = 4$ N) and the slip distance $d_s = 9.6$ m.

$$K_V = \frac{V}{d_s.F_N} \tag{9}$$

The average wear rate calculated for each sample shows 2.9×10^{-4} $mm^3/N.m$ and 3.2×10^{-4} $mm^3/N.m$ for doped and undoped steels, respectively. There is no significant difference between the two samples. However, the influence of powder particle size relative to the contact size on wear behavior has not been evaluated, even though both are of the same order of magnitude. Additional investigations would likely be necessary to explore this aspect, alongside an understanding of the subsurface deformation mechanisms, particularly in the region of

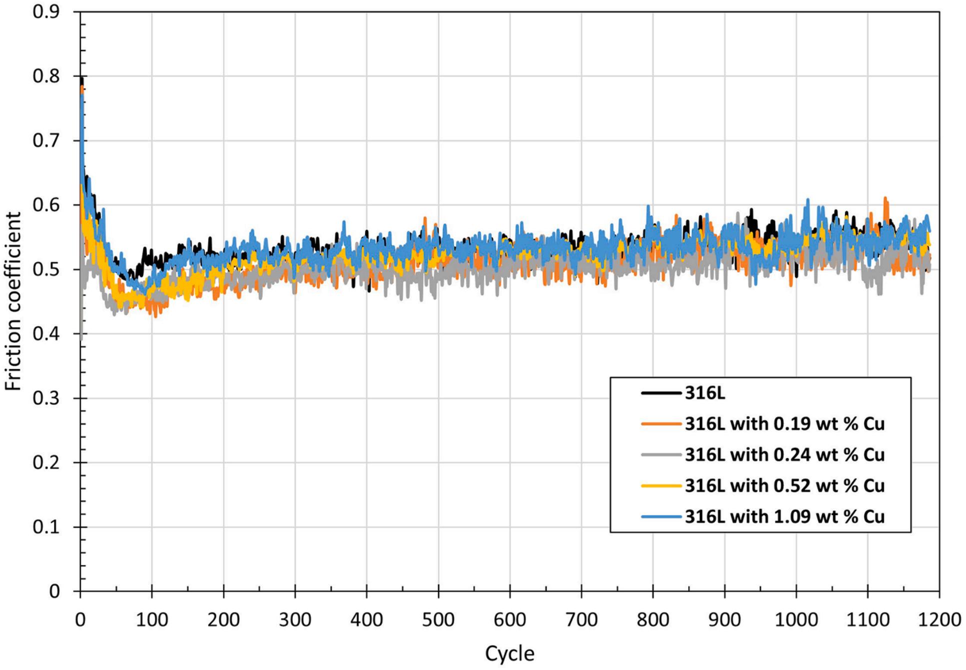

Fig. 12. Graphical representation of the evolution of the friction coefficient as a function of the number of cycles during the tribology tests.

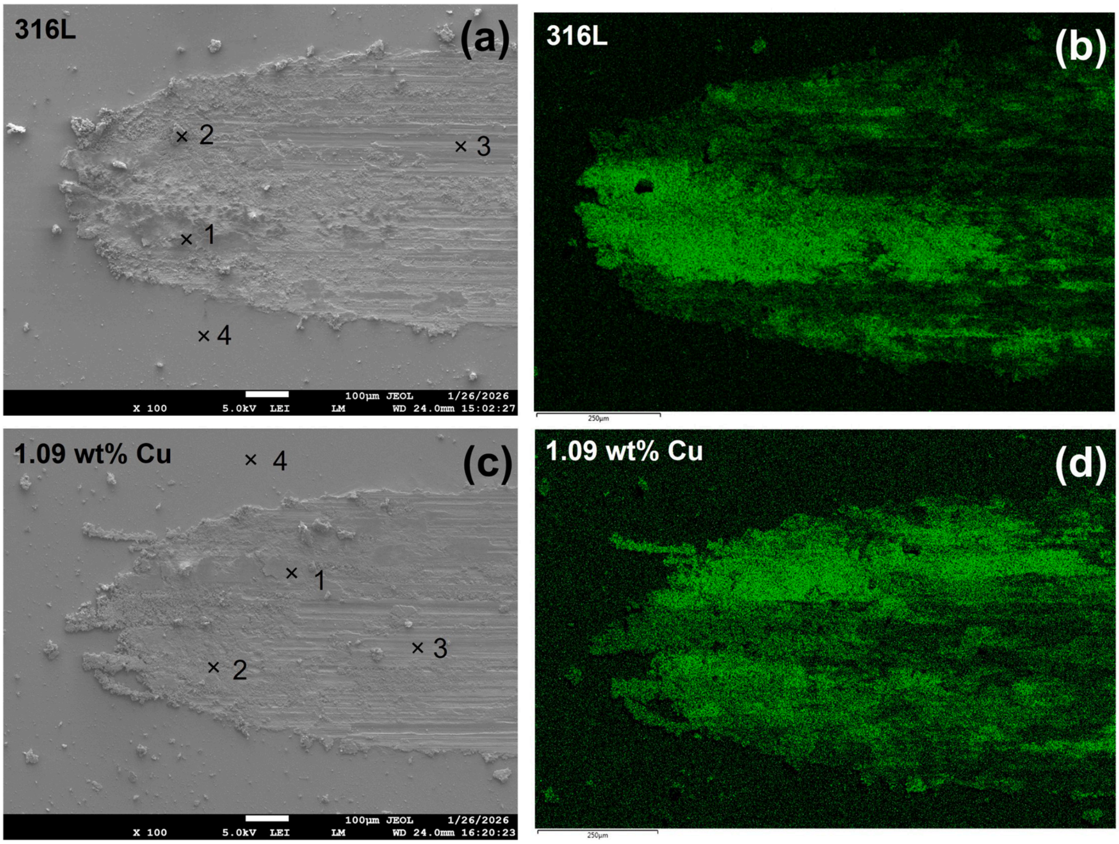

Fig. 13. SEM images and EDS maps of oxygen in the wear track of the sintered materials: (a) and (b) 316 L; (c) and (d) 316 L containing 1.09 wt.% Cu.

maximum shear.

Table 2
Mass composition of the different areas analyzed by EDS on the wear tracks shown in Fig. 13.

Test Zones (wt.%)	O	Si	Cr	Mn	Fe	Ni	Mo	Cu
316L – Zone 1	29.5 ± 1.4	0.6 ± 0.1	12.5 ± 1.4	1.0 ± 0.5	45.5 ± 0.1	9.0 ± 0.1	1.9 ± 0.3	
316L – Zone 2	24.5 ± 5.7	0.9 ± 0.3	16.0 ± 3.3	2.7 ± 1.7	43.8 ± 3.1	8.6 ± 0.8	3.5 ± 1.4	
316L – Zone 3	3.1 ± 1.1	0.7 ± 0.0	19.4 ± 1.8	1.3 ± 0.8	59.0 ± 2.4	12.6 ± 1.4	3.9 ± 2.2	
316L – Zone 4	0.5 ± 0.1	0.8 ± 0.1	18.6 ± 0.4	1.4 ± 0.7	61.6 ± 0.2	14.6 ± 0.3	2.5 ± 0.5	
1.09 wt. %Cu – Zone 1	27.5 ± 0.6	0.6 ± 0.1	12.3 ± 0.5	0.1 ± 0.0	46.0 ± 0.1	10.7 ± 0.1	2.2 ± 0.2	0.6 ± 0.1
1.09 wt. %Cu – Zone 2	12.5 ± 5.4	0.8 ± 0.1	15.5 ± 1.8	2.1 ± 0.8	53.4 ± 4.2	12.3 ± 1.4	2.7 ± 0.8	0.7 ± 0.3
1.09 wt. %Cu – Zone 3	4.2 ± 2.6	0.9 ± 0.3	19.2 ± 2.1	2.1 ± 1.3	56.9 ± 5.7	12.8 ± 2.9	3.7 ± 2.3	0.2 ± 0.2
1.09 wt. %Cu – Zone 4	0.5 ± 0.1	0.7 ± 0.1	18.6 ± 0.5	1.9 ± 1.1	60.5 ± 2.8	14.0 ± 0.5	2.7 ± 0.2	1.1 ± 0.5

4. Conclusions

In this study an innovative hybrid approach combining physical vapor deposition and (PVD) and Spark Plasma Sintering (SPS) processes was used to produce a 316L/Cu composite. The key findings are summarized as follow:

- The PVD setup enables a homogeneous and reproducible coating, with a linear deposition rate over time (16.3 nm/h).
- XRD analyses reveals austenitic phase in all samples. A shoulder associated with the copper peak is visible in the coated powder and disappears after sintering.
- EDS analyses shows preferential diffusion of Ni and Mn into the Cu-rich areas during sintering.
- Adding copper beyond 0.52 wt.% leads to an increase in the elongation at break of the sintered specimens. However, the sintering conditions are not optimal, as fracture surfaces still show partially unbonded powder particles.
- Hardness tends to slightly decrease with copper addition, but copper helps reduce porosity—except at low contents.
- The addition of 1.09 wt.% copper does not appear to alter the wear behavior of the steel.
- This processing route combining PVD and SPS offers precise control over the nature and amount of elements at powder particle boundaries, enabling optimization of the material's properties.

CRediT authorship contribution statement

Yoann Pinot: Writing – original draft, Supervision, Methodology, Investigation, Conceptualization. **Romaric Masset:** Investigation. **Aurélien Besnard:** Writing – review & editing, Investigation. **Rémi Aubert:** Writing – review & editing, Investigation. **Guillaume Colas:**

Writing – review & editing, Investigation. **Maria-Rosa Ardigo-Besnard:** Writing – review & editing, Investigation. **Florian Bussière:** Investigation.

Declaration of competing interest

The authors declare that they have no known competing financial interests or personal relationships that could have appeared to influence the work reported in this paper.

Acknowledgement

This work is partly supported by the French RENATECH network through its FEMTO-ST Technological facilities MIMENTO.

Data availability

Data will be made available on request.

References

[1] Y. Jiang, J.F. Yang, Z. Zhuang, R. Liu, Y. Zhou, X.P. Wang, Q.F. Fang, Characterization and properties of tungsten carbide coatings fabricated by SPS technique, J. Nucl. Mater. 433 (2013) 449–454, https://doi.org/10.1016/j.jnucmat.2012.10.020.

[2] K.A. Khor, L.G. Yu, G. Sundararajan, Formation of hard tungsten boride layer by spark plasma sintering boriding, Thin. Solid. Films. 478 (2005) 232–237, https://doi.org/10.1016/j.tsf.2004.07.004.

[3] J.H. Yan, Y. Wang, L.F. Liu, Y. Wang, Oxidation and interdiffusion behavior of niobium substrate coated $MoSi_2$ coating prepared by spark plasma sintering, Appl. Surf. Sci. 320 (2014) 791–797, https://doi.org/10.1016/j.apsusc.2014.09.018.

[4] H.G. Mohammed, T.M.B. Albarody, M. Mustapha, N.M. Sulan, Al-Jothery HKM, Effect of process parameters of magnetic-inductively assisted SPS of Fe_3O_4 on microstructure behavior—Part I, Mater. Today Proc. 42 (2021) 2106–2112, https://doi.org/10.1016/j.matpr.2020.12.293.

[5] J. Wu, X. An, J. Zhang, S. Lei, Y. Guo, X. Xu, W. Yao, Q. Wang, Q. Kong, Effect of mechanical alloying on microstructure and mechanical properties of Ti-24Nb-4Zr-3Mn alloys prepared by SPS, J. Alloys. Compd. 927 (2022) 167023, https://doi.org/10.1016/j.jallcom.2022.167023.

[6] B.A. Obadele, O.S. Adesina, O.P. Oladijo, E.N. Ogunmuyiwa, Fabrication of functionally graded 316L austenitic and 2205 duplex stainless steels by spark plasma sintering, J. Alloys. Compd. 849 (2020) 156697, https://doi.org/10.1016/j.jallcom.2020.156697.

[7] M. Beyhadhi, A.R. Kiani-Rashid, M. Kashefi, J.V. Khaki, S. Jonsson, Effect of powder reactivity on fabrication and properties of NiAl/Al_2O_3 composite coated on cast iron using SPS, Appl. Surf. Sci. 344 (2015) 1–8, https://doi.org/10.1016/j.apsusc.2015.01.186.

[8] X. Ji, J. Zhao, H. Wang, C. Luo, Sliding wear of SPS CrFeCoNiCu high-entropy alloy coatings with MoS_2 and WC additions, Int. J. Adv. Manuf. Technol. 96 (2018) 1685–1691, https://doi.org/10.1007/s00170-017-0794-z.

[9] S.X. Song, Z. Wang, G.P. Shi, Heating mechanisms of spark plasma sintering, Ceram. Int. 39 (2013) 2437–2442, https://doi.org/10.1016/j.ceramint.2012.08.095.

[10] M.R. Ardigo-Besnard, A. Besnard, Y. Pinot, F. Bussière, J.P. Chateau-Cornu, C. Vandenabeele, S. Lucas, N. Watiez, A. Descamps-Mandine, G. Josse, A. Proietti, Austenitic-to-austenitic-ferritic stainless steel transformation via PVD powder surface functionalization and SPS, Materialia 33 (2024) 102002, https://doi.org/10.1016/j.mtla.2023.102002.

[11] A. Kumar, O. Vichare, K. Debnath, M. Paswan, Fabrication methods of metal matrix composites (MMCs), Mater. Today Proc. 46 (2021) 2764–2769, https://doi.org/10.1016/j.matpr.2021.02.511.

[12] T.K. Kandavel, R. Chandramouli, M. Manoj, B. Manoj, D.K. Gupta, Influence of copper and molybdenum on dry sliding wear behaviour of sintered plain carbon steel, Mater. Des. 50 (2013) 667–673, https://doi.org/10.1016/j.matdes.2013.03.053.

[13] S. Mirzababaei, V.V.K. Doddapaneni, K. Lee, G.E. Paul, H. Pirgazi, K.S. Tan, O. Ertorer, C.H. Chang, B.K. Paul, S. Pasebani, Enhancement in thermal conductivity of stainless steel via LPBF 316L-Cu composite, Addit. Manuf. 70 (2023) 103576, https://doi.org/10.1016/j.addma.2023.103576.

[14] H. Zhao, Y. Ding, J. Li, G. Wei, M. Zhang, Corrosion resistance of laser-melting-deposited Cu-bearing 316L stainless steel in 0.5 M H_2SO_4, Mater. Chem. Phys. 291 (2022) 126572 https://doi.org/10.1016/j.matchemphys.2022.126572.

[15] M. Kultamaa, M. Gunell, K. Mönkkönen, M. Suvanto, J.J. Saarinen, Antimicrobial activity of porous MIM 316L stainless steel by Zn, Cu and Ag electrodeposition, Surf. Interfaces. 38 (2023) 102778, https://doi.org/10.1016/j.surfin.2023.102778.

[16] W.D. Wong-Angel, L. Tellez-Jurado, J.F. Chavez-Alcala, E. Chavira-Martinez, Verduzco-Cedeno VF, Effect of copper on mechanical properties of PM alloys, Mater. Des. 57 (2014) 250–257, https://doi.org/10.1016/j.matdes.2014.01.008.

[17] R.F. Vaz, A. Garfias, V. Albaladejo, J. Sanchez, I. Garcia Cano, Advances in cold spray additive manufacturing: a review, Coatings 13 (2023) 267, https://doi.org/10.3390/coatings13020267.

[18] P. Lin, L. Wang, X. Liang, Q. Hu, L. Wang, Effects of copper infiltrant amount and infiltration method on mechanical properties of sintered steel, J. Phys. Conf. Ser. 2690 (2024) 012005, https://doi.org/10.1088/1742-6596/2690/1/012005.

[19] C.R. Vandenabeele, S. Lucas, Technological challenges and progress in nanomaterials plasma surface modification: a review, Mater Sci Eng R 139 (2020) 100521, https://doi.org/10.1016/j.mser.2019.100521.

[20] J. Zhou, Y. Ji, H. Bai, X. Dong, X. Kang, Y. Li, Factors controlling evolution of nanoscale oxides in 316L stainless steel manufactured by LPBF, Mater. Sci. Eng. A 942 (2025) 148682, https://doi.org/10.1016/j.msea.2024.148682.

[21] A.B. Kale, A. Bag, J.H. Hwang, E.G. Castle, M.J. Reece, S.H. Choi, Deformation and fracture behaviors of SPS-fabricated 316L stainless steels, Mater. Sci. Eng. A 707 (2017) 287–294, https://doi.org/10.1016/j.msea.2017.09.063.

[22] H. Kurgan, R. Varol, Mechanical properties of P/M 316L stainless steel materials, Powder. Technol. 202 (2010) 71–77, https://doi.org/10.1016/j.powtec.2010.04.012.

[23] G. Marnier, C. Kelier, J. Noudem, E. Hug, Functional properties of SPS ultrafine-grained 316L, Mater. Des. 63 (2014) 419–426, https://doi.org/10.1016/j.matdes.2014.06.013.

[24] B. Deepanraj, N. Senthilkumar, T. Tamizharasan, Effect of sintering parameters on microstructure and hardness of copper alloy, Mater. Today Proc. 80 (2023) 2468–2473, https://doi.org/10.1016/j.matpr.2022.12.356.

[25] N. Kurgan, Effect of porosity and density on mechanical and microstructural properties of sintered 316L implant materials, Mater. Des. 56 (2014) 185–192, https://doi.org/10.1016/j.matdes.2013.10.082.

[26] K. Lokeshraj, K.G. Prashanth, A.K. Jeevanantham, 316L stainless steel fabricated by SLM and SPS: microstructural, mechanical and electrochemical comparison, J. Mater. Res. Technol. 40 (2026) 2868–2875, https://doi.org/10.1016/j.jmrt.2023.12.145.

[27] B. Flipon, C. Keller, L. Garcia de la Cruz, E. Hug, F. Barbe, Tensile properties of SPS AISI 316L with unimodal and bimodal grain size distributions, Mater. Sci. Eng. A 729 (2018) 185–195, https://doi.org/10.1016/j.msea.2018.05.052.

[28] K.D. Christian, R.M. German, Relation between pore structure and fatigue behavior in sintered Fe–Cu–C alloys, Int J Powder Metall 31 (1995) 51–61.

[29] J.Y. Sun, L.C. Zhang, R. Liu, Z.M. Xie, J.F. Yang, X.F. Xie, X.P. Wang, Q.F. Fang, C. S. Liu, X. Wu, Effect of Mo nanoparticles on microstructure and mechanical properties of Cu alloys by self-propagating and SPS, Mater. Sci. Eng. A 916 (2024) 147305, https://doi.org/10.1016/j.msea.2024.147305.

[30] Y. Pinot, A. Besnard, M.R. Ardigo-Besnard, F. Bussière, 316L stainless-steel carburizing near eutectic transformation using SPS, J. Mater. Eng. Perform. 34 (2025) 3937–3948, https://doi.org/10.1007/s11665-024-09386-7.